RESEARCH ARTICLE

Key Points:
- Our net basal melt rate estimate is 57.4 ± 25.3 Gt yr^{-1} (1 ± 0.4 m yr^{-1}) larger than previous modeling-based and glaciological-based estimates
- The Mackenzie polynya controls the seasonal exchange of dense waters into the ice shelf cavity
- SW controls the formation rate and thermohaline properties of DSW formed by the Mackenzie polynya

Basal melt, seasonal water mass transformation, ocean current variability, and deep convection processes along the Amery Ice Shelf calving front, East Antarctica

L. Herraiz-Borreguero[1,2,3], J. A. Church[4], I. Allison[1], B. Peña-Molino[1], R. Coleman[1,5], M. Tomczak[6], and M. Craven[1]

[1]Antarctic Climate and Ecosystem Cooperative Research Centre, University of Tasmania, Hobart, Tasmania, Australia, [2]Centre for Ice and Climate—Niels Bohr Institute, University of Copenhagen, Copenhagen, Denmark, [3]Now at National Oceanographic Center, University of Southampton, Southampton, UK, [4]CSIRO Oceans and Atmosphere Flagship, Hobart, Tasmania, Australia, [5]Institute for Marine and Antarctic Studies, University of Tasmania, Hobart, Tasmania, Australia, [6]School of the Environment, Flinders University of South Australia, Adelaide, South Australia, Australia

Abstract Despite the Amery Ice Shelf (AIS) being the third largest ice shelf in Antarctica, the seasonal variability of the physical processes involved in the AIS-ocean interaction remains undocumented and a robust observational, oceanographic-based basal melt rate estimate has been lacking. Here we use year-long time series of water column temperature, salinity, and horizontal velocities measured along the ice shelf front from 2001 to 2002. Our results show strong zonal variations in the distribution of water masses along the ice shelf front: modified Circumpolar Deep Water (mCDW) arrives in the east, while in the west, Ice Shelf Water (ISW) and Dense Shelf Water (DSW) formed in the Mackenzie polynya dominate the water column. Baroclinic eddies, formed during winter deep convection (down to 1100 m), drive the inflow of DSW into the ice shelf cavity. Our net basal melt rate estimate is 57.4 ± 25.3 Gt yr^{-1} (1 ± 0.4 m yr^{-1}), larger than previous modeling-based and glaciological-based estimates, and results from the inflow of DSW (0.52 ± 0.38 Sv; 1 Sv $= 10^6$ m^3 s^{-1}) and mCDW (0.22 ± 0.06 Sv) into the cavity. Our results highlight the role of the Mackenzie polynya in the seasonal exchange of water masses across the ice shelf front, and the role of the ISW in controlling the formation rate and thermohaline properties of DSW. These two processes directly impact on the ice shelf mass balance, and on the contribution of DSW/ISW to the formation of Antarctic Bottom Water.

1. Introduction

Ice shelves are areas of thick floating ice that extend from an ice sheet into the ocean. Around Antarctica, they are the primary regions where the ice sheet discharges into the Southern Ocean. Ice shelves act as buttresses for the Antarctic Ice Sheet, and the current widespread and intensifying glacier acceleration along some Antarctic coastal margins has been linked to the destabilization of the ice shelves by basal melt [*Joughin et al.*, 2014]. Thinner ice shelves are less capable of restraining the flow of the glaciers which feed them, thus further increasing the ice discharge to the ocean [*Bamber and Aspinall*, 2013] and resulting in increased sea level rise (SLR). Since the early 1990s, the contribution of the Antarctic Ice Sheet to SLR has accelerated, accounting now for $\sim$10% of the total rate [*Church et al.*, 2013]. Recent work [*Pritchard et al.*, 2012] points to increased heat transport by the ocean to the base of the ice shelves as the primary cause of this acceleration, but the ocean dynamics driving this increased heat delivery are poorly understood.

The Amery Ice Shelf (60°E–70°E), with an area of $\sim$62,000 km^2, is the third largest embayed ice shelf in Antarctica and the largest in East Antarctica (Figure 1). Although small compared with the Ross and the Filchner-Ronne ice shelves, the Amery Ice Shelf is fed by the Lambert Glacier system which drains $\sim$16% of the area of East Antarctica [*Allison*, 1979]. Over the past decades, monitoring the ocean underneath the Amery Ice Shelf has been an important objective of the Amery Ice Shelf-Ocean Research (AMISOR) Project. While significant data sets have been collected from beneath ice shelves in West Antarctica [e.g., *Clough and Hansen*, 1979; *Foster*, 1983; *Jacobs et al.*, 1979; *Nicholls and Jenkins*, 1993], the AMISOR Project has provided the first comprehensive data set for investigation of ice shelf-ocean interactions in East Antarctica. The data, collected since 2001 (and ongoing) includes oceanographic moorings in boreholes through the
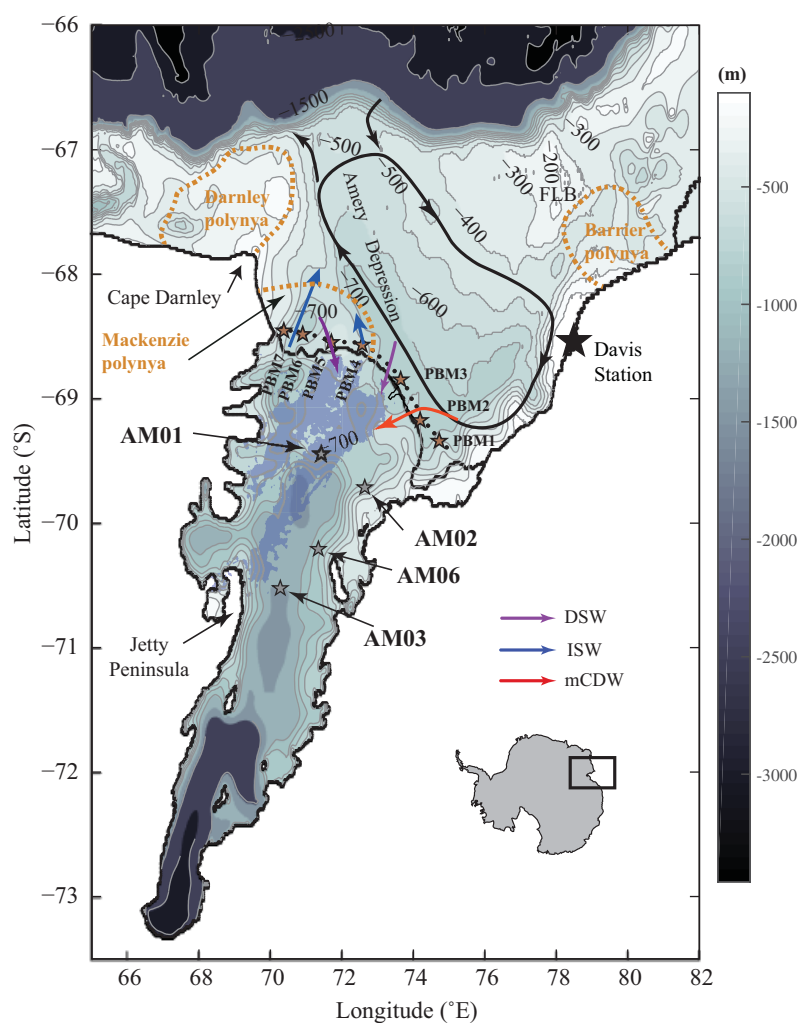
Figure 1. Map showing the location of the seven moorings, PBM1-7, along the ice shelf front (brown stars) and four boreholes sites, AM01, AM02, AM03, and AM06 (grey stars), and the main environmental features in the vicinity of the Amery Ice Shelf. Orange dashed lines delimit the location of the Darnley, Barrier, and Mackenzie polynyas, and black thick lines show the general ocean circulation in Prydz Bay, and in color, the main inflow/outflow paths across the ice shelf front. The blue shaded area shows the area of refreezing where the marine ice layer is 50–200 m thick. The contour shows the bathymetry. Inset: location of the Amery Ice Shelf in East Antarctica.

ice shelf and off the ice shelf front (discussed in the present article), sediment cores, glacial and marine ice samples, ocean currents, thermistors, and fiber-optic ice/ocean temperature measurements, in addition to a wide range of glaciological and geophysical measurements.

The ocean circulation in Prydz Bay consists of a large cyclonic gyre, centered in a deep channel, known as the Amery Depression [*Nunes Vaz and Lennon*, 1996; *Smith et al.*, 1984]. The gyre is associated with a relatively narrow coastal current that runs along the Amery Ice Shelf calving front, and continues westward after leaving Prydz Bay (Figure 1). The flow becomes very strong along the western side of Prydz Bay, with speeds exceeding 1 m s^{-1} [*Nunes Vaz and Lennon*, 1996]. Several regional studies have modeled the ocean circulation in Prydz Bay and beneath the Amery Ice Shelf [e.g., *Williams et al.*, 2001; *Galton-Fenzi et al.*, 2012]. They all reproduce the cyclonic gyre of Prydz Bay, and suggest a similar cyclonic circulation beneath the ice shelf (i.e., inflow of shelf waters in the east and outflow of Ice Shelf Water (ISW) and marine ice formation in the west). Model results also suggest that the Prydz Bay gyre is not persistent over time [*Galton-Fenzi et al.*, 2012].

This cyclonic circulation drives the inflow of modified Circumpolar Deep Water (mCDW) along the eastern flank of the Amery Ice Shelf calving front. *Herraiz-Borreguero et al.* [2015] used a wide range of oceanographic data to describe the interaction of mCDW with the Amery Ice Shelf. Using temperature-salinity

profiles from instrumented elephant seals, they showed that mCDW occupies the eastern flank of Prydz Bay and reaches the ice shelf at the beginning of the austral winter. mCDW enters the ice shelf cavity, causing a basal melt of up to 2 m yr^{-1} under the eastern corner of the ice shelf base [*Herraiz-Borreguero et al.*, 2015]. Heat content associated with mCDW inflows observed ∼80 km inward from the ice shelf front showed large inter-annual variability in the ocean heat content of up to −40% in 2004–2005 compared to 2001, comparable to that documented in the Amundsen Sea [*Dutrieux et al.*, 2014].

ISW forms from the interaction of the ocean with the ice shelf. As a result, ISW has a temperature below the surface freezing point (typically $< -1.95°$C). The excess buoyancy of the ISW due to the meltwater component causes it to ascend along the upward-sloping base of the ice shelf. As ISW rises, its temperature might become less than the in situ freezing point, which is rising due to the reducing pressure [*Foldvik and Kvinge*, 1974]. This can result in the formation of frazil ice crystals, which can accrete at the ice shelf base and form a layer of marine ice.

The marine ice layer under the Amery Ice Shelf [*Morgan*, 1972; *Fricker et al.*, 2001] is an important feature of its overall structure, and is an important factor in ice shelf stability, both because its presence affects ice shelf flow and mechanical properties [*Craven et al.*, 2009], and due to its interaction with fracture features [*Khazendar et al.*, 2001, 2009]. The marine ice layer is up to 190 m thick and accounts for 9% of the ice shelf volume; this layer occupies the north-western sector of the Amery Ice Shelf and extends all the way to the calving front [*Fricker et al.*, 2001]. The formation of frazil ice, and deposition under the ice shelf base, is subject to seasonal variability [*Herraiz-Borreguero et al.*, 2013], and the frazil ice crystals are responsible for the lifting of mooring arrays (AM01, AM04, and AM05), deployed in the Amery Ice Shelf cavity [*Craven et al.*, 2014].

The topography of the Lambert Glacier basin shapes the large-scale wind circulation pattern near the surface. The winds wrap around the Lambert Glacier basin, with velocities in excess of 10 m/s, with little seasonal variability in the wind direction [*van den Broeke and van Lipzig*, 2003]. These winds are responsible for the formation (and maintenance) of three coastal polynyas within Prydz Bay. These are, clockwise from the northeast, the Barrier, Mackenzie, and Darnley polynyas (Figure 1).

The occurrence of coastal polynyas within Prydz Bay plays a key role in the sea ice and Dense Shelf Water (DSW) formation. The Barrier polynya occurs on the northeastern side of Prydz Bay, close to the continental shelf break, and it is responsible for an average cumulative annual sea ice production of 80.0 ± 19 km^3 (for an average area of 6.0 ± 2.7 10^3 km^2) [*Tamura et al.*, 2008]. The Mackenzie polynya occurs on the western flank of the Amery calving front (Figure 1) and it is responsible for an average cumulative annual sea ice production of 68.2 ± 5.8 km^3 (for an average area of 3.9 ± 2.1 10^3 km^2) [*Tamura et al.*, 2008]. Both these polynyas are linked to the formation of DSW, which, together with the DSW formed in the Darnley polynya, ultimately contributes to the formation of Cape Darnley Bottom Water (G. D. Williams, personal communication).

This paper documents the interaction of the ocean with the Amery Ice Shelf on intra-annual times scales and builds on the results shown by *Leffanue and Craven* [2004]. For this purpose, we use a year-long time series of ocean temperature, salinity, and horizontal velocity collected along the ice shelf calving front. This paper is organized as follows: section 2 shows the design and instrumentation of the oceanographic moorings; section 3 focuses on the description of the observed water masses and their seasonal variability, together with the ocean currents; in section 4, we discuss the variability of the ocean currents and, in particular, the formation of DSW through deep convection driven by the Mackenzie polynya. Finally, ice shelf basal melt estimates are discussed, followed by conclusions in section 5.

2. Data

The mooring array consists of seven moorings, hereafter Prydz Bay Moorings (PBM1 to 7), measuring temperature, salinity, and horizontal velocity. These were deployed along the whole calving front of the Amery Ice Shelf from February 2001 to February 2002 (Figure 1). The ice shelf is approximately 350 m thick at the calving front, which is ∼200 km long. The distance between moorings was on average 34 km, and they cover the ice shelf front. The moorings were equipped with 27 thermosalinographs, 5 temperature loggers, 25 rotor current meters, 1 acoustic current meter, and 4 acoustic Doppler current profilers
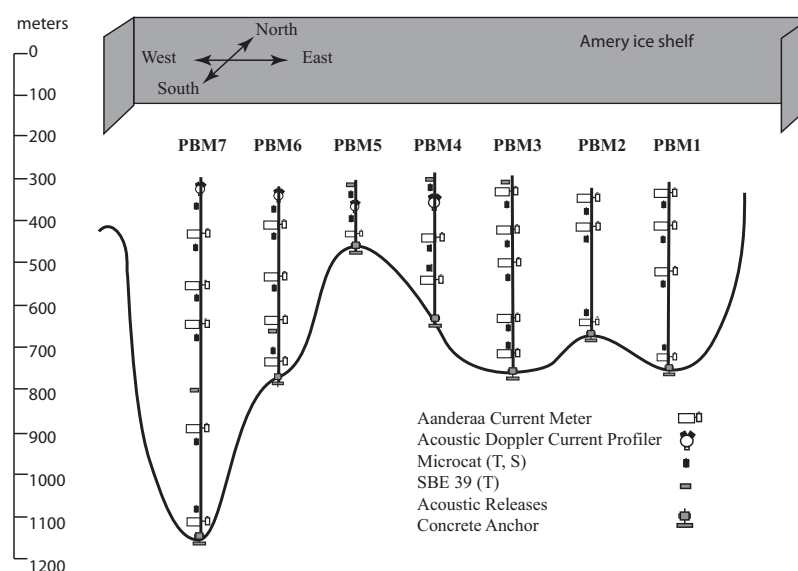
Figure 2. Design of the PBM mooring array along the Amery Ice Shelf front.

(RDI Broadband 150 kHz ADCP) (Figure 2). See Table 1 for specific details on instrument location and depth. Temperature and salinity were recorded every 5 min, while velocity (including ADCP velocity) was recorded every 60 min. An exception was the current meter RCM9-597_9 on PBM7 (Table 1), which recorded velocity every 20 min.

3. Results

3.1. Water Masses Interacting With the Amery Ice Shelf

The high spatial resolution of the moorings and the large spatial extent of the water masses, described next, allows the construction of monthly mean sections of temperature and salinity. We show the temperature and the salinity sections in July (Figures 3a and 3b) and December (Figures 3c and 3d) to highlight the spatial and seasonal characteristics of the water masses along the ice shelf front. Two features stand out, (i) the presence of relatively warm water on the eastern flank of the calving front during the austral winter (Figure 3a), while cold and saltier waters occupy the western flank all-year-round, with the highest-salinity water in the austral summer (Figure 3d); and (ii), the increased horizontal salinity (density) gradient along the ice shelf in the austral summer (Figure 3d). To distinguish these east-to-west differences along the ice shelf front, we will group the PBMs as follows: PBMs 1–3 (east) and PBMs 4–7 (west). We will follow this zonal arrangement throughout the paper.

Three main water masses are known to play a key role in the interaction of the ocean with the Amery Ice Shelf: modified Circumpolar Deep Water (mCDW), Dense Shelf Water (DSW), and Ice Shelf Water (ISW). These are described in detail next.

3.1.1. Modified Circumpolar Deep Water (mCDW)

CDW is the warmest subsurface water mass offshore the Antarctic continental shelf. In some areas, modified CDW is able to get on to the continental shelf. We define mCDW as a water mass with potential temperature, θ, of $-0.5 \leq \theta \leq -1.85°C$ and a neutral density (γ^n) of $28.0 < \gamma^n < 28.27$ kg m^{-3}. Its seasonal inflow is mostly captured by the three eastern-most moorings, PBM1 to PBM3. *Herraiz-Borreguero et al.* [2015] documents the interaction of mCDW with the AIS in detail using moorings PBM1-3 and a mooring deployed in the ice shelf cavity. Here we repeat the main points highlighted in their paper. mCDW is first observed on the eastern flank of the Amery calving front by the end of February 2001 at PMB1, followed by PBM2 and PBM3 (Figures 4a–4c). The highest temperature observed in these three PBM moorings along the ice shelf front peaks at 330–465 dbar in May ($-1.4°C$) and, at ~575 dbar in July ($-1.53°C$; seen in the unfiltered time series). In the west, mCDW is essentially absent and only observed sporadically, e.g., around June in PBM4

Table 1. Summary of Mooring Details[a]

Mooring	Latitude (South)	Longitude (East)	Ocean Depth (m)	Instrument	Instrument Depth (m)	Deployment/Recovery Date
PBM 1	69°22.014′	74°38.153′	750	RCM8-10867	367	16 Feb 2001 to 22 Feb 2002
				microCAT-315	368	
				RCM8-10919	459	
				microCAT-316	460	
				RCM8-10282	**571**	
				microCAT-317	572	
				microCAT-318	**725**	
PBM 2	69°12.001′	74°05.962′	672	RCM8-10868	370	16 Feb 2001 to 1 Feb 2002
				microCAT-319	371	
				RCM8-10993	**462**	
				microCAT-320	463	
				microCAT-321	647	
				RCM8-10917	657	
PBM 3	68°52.386′	73°33.310′	768	SBE39-089	324	17 Feb 2001 to 21 Feb 2002
				RCM8-10914	347	
				microCAT-322	**348**	
				RCM8-10869	439	
				microCAT-323	**440**	
				RCM8-10996	551	
				microCAT-324	552	
				RCM8-10311	**663**	
				microCAT-325	664	
				microCAT-326	743	
				RCM5-8670x	753	
PBM 4	68°35.314′	72°30.236′	538	SBE39-107	347	17 Feb 2001 to 12 Feb 2002
				microCAT-327	366	
				ADCP-0136	367	
				RCM8-10915	**459**	
				microCAT-328	**460**	
				microCAT-329	513	
				RCM8-10768	523	
PBM 5	68°34.840′	71°39.816′	472	SBE39-112	345	17 Feb 2001 to 10 Feb 2002
				microCAT-330	364	
				ADCP-1136	365	
				microCAT-332	447	
				RCM8-10704	457	
PBM 6	68°30.330′S	70°51.770′E	786	**ADCP-0135**	**365**	18 Feb 2001 to 11 Feb 2002
				microCAT-380	366	
				RCM8-10916	457	
				microCAT-908	458	
				RCM8-10284	569	
				microCAT-909	570	
				RCM8-10701	681	
				SBE39-111	682	
				microCAT-911	761	
				RCM8-10703	**771**	
PBM 7	68°28.659′	70°23.118′	1135	**ADCP-1143**	**378**	18 Feb 2001 to 11 Feb 2002
				microCAT-912	379	
				RCM8-10918	470	
				microCAT-913	471	
				RCM8-7838x	582	
				microCAT-914	583	
				RCM8-10998	**694**	
				microCAT-1119	695	
				SBE39-115	805	
				RCM8-10702	906	
				microCAT-1120	907	
				microCAT-1121	1110	
				RCM9-597_9	**1120**	

[a]Instruments in bold are incomplete or showed some biased.

and PBM5 (Figures 5a and 5b). Oceanographic instruments attached to elephant seals also show that mCDW is confined to the eastern side of the domain [*Herraiz-Borreguero et al.*, 2015].

3.1.2. Dense Shelf Water (DSW)

DSW usually refers to the densest water mass on the Antarctic continental shelf. DSW forms when brine is rejected during sea ice formation and mixes with the ocean, especially under polynyas [e.g., *Ohshima et al.*,
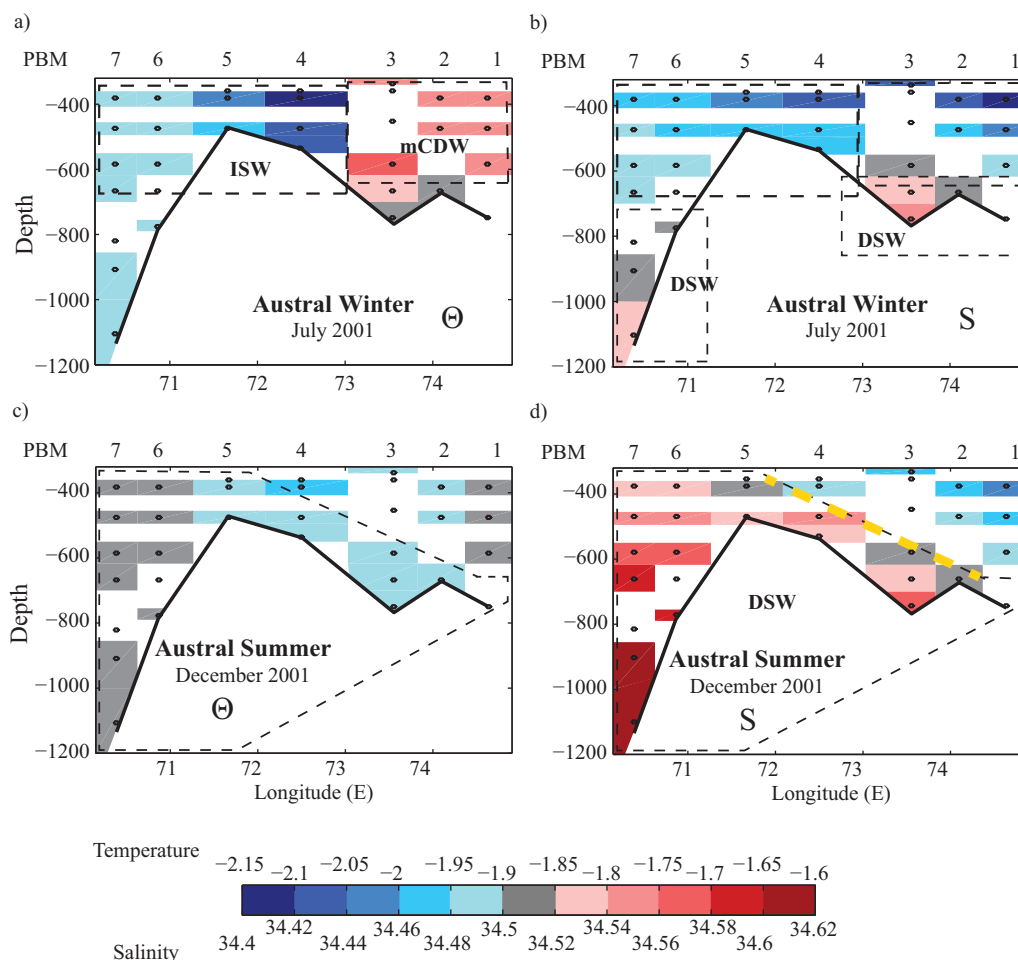
Figure 3. Monthly mean sections of (a, c) potential temperature and (b, d) salinity during the austral (a, b) winter (July) and (c, d) summer (December). The area occupied by the three main water masses found along the section is delimited by a polygon. The water masses are: ISW, Ice Shelf Water; DSW, Dense Shelf Water; and mCDW, modified Circumpolar Deep Water. The black dashed line shows the slope of the 34.5 isohaline in summer. The location of the instruments is shown as a black dot.

2013]. DSW is defined here as a water mass with salinity, S, greater or equal to 34.5, and potential temperature, θ, ranging from $-1.85°C$ to $-1.95°C$ (just below the surface freezing temperature of $-1.89°C$). We have chosen a temperature lower than the surface freezing point to account for the mixing of DSW with ISW at the ice shelf front (section 4).

DSW is observed all year round, but there are zonal differences along the ice shelf front. In the east, DSW is observed at the bottom of the water column, below ~600 m at PBM3 (Figure 4f). These eastern mooring sites are within the deepest part of the Amery Depression (Figure 1) near the ice shelf front. Failure in the bottom (temperature and salinity) sensors at PBM1 means there is no direct evidence of DSW at these locations (Figures 4a and 4d). However, a few features do support the presence of DSW at these sites: the temperature at ~660 m in PBM2 and PBM3 are of the same range and seasonal variability; and, the deepest records available in PBM1 and PBM2 lie within the 34.5 limit. In the west, DSW is observed below ~600 m, and throughout the whole water column during the austral winter, especially at PBM6 and PBM7, where the densest DSW is found within the area of the Mackenzie polynya (Figure 5).

A common feature observed along the ice shelf calving front is a gradual freshening in the austral summer, followed by a gradual increase in salinity during the austral winter resulting from sea ice formation and the associated brine rejection. However, large zonal differences are observed, especially at the onset of the salinity increase. In the east, the onset of the salinity increase (followed by a gradual cooling toward the surface freezing temperature) starts in July at all depths above ~600 m, and it is amplified at shallower depths
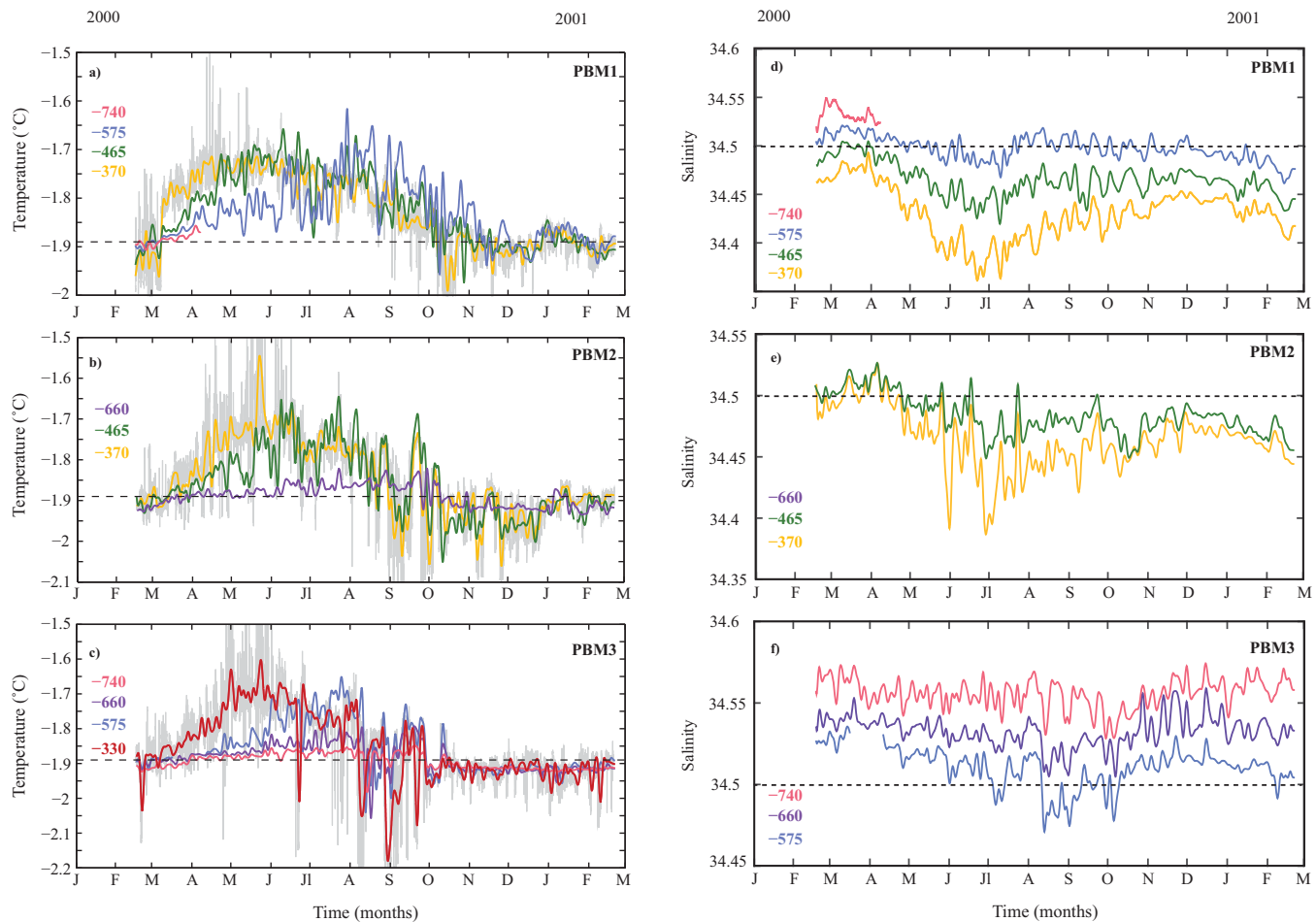
Figure 4. Time series of potential temperature at (a) PBM1, (b) PBM2, and (c) PBM3. The times series have been filtered using a 48 h low-pass Butterworth filter. Each time series is color coded according to a nominal depth at which the measurements were sampled. The exact depth of the time series is shown in Table 1. The freezing temperature at the ocean surface is shown as a horizontal black dash line. The unfiltered time series of temperature is shown for the shallowest microCAT in grey. Note that the vertical axes have different temperature range. Time series of salinity at (d) PBM1, (c) PBM2, and (f) PBM3. As in Figures 4a–4c. The 34.5-isohaline is shown as a horizontal dashed line. Note that the vertical axes have different salinity range.

(Figures 4d–4f). Below this depth, at PBM3, the seasonal cycle is very weak, and a slight increase in salinity is only hinted at between August and October (Figure 4f, purple and pink). In the west, the onset of the salinity increase is around May at depths shallower than 600 m in PBM6 and PBM7 and August in PBM4 to PBM5 (Figure 5). This salinity increase is also followed by a warming toward the surface freezing point. The surface freezing point is reached progressively from west to east, between July and September (Figures 4a–4c and 5a–5d). In section 4, we will show that the outflow of ISW during active sea ice formation delays the formation of DSW.

3.1.3. Ice Shelf Water (ISW)

ISW forms when the ocean drives melting at the base of an ice shelf typically at several hundred meters depth. ISW is characterized by temperatures below the surface freezing point, thus we define ISW as the water mass with $\theta \leq -1.95°C$.

ISW is the dominant water mass at intermediate depths on the western flank of the ice shelf calving front. In the east, ISW is sporadically observed at mid depths ($\sim$450 m) in February and from August to December (Figures 4a–4c). This ISW is slightly warmer and saltier ($\overline{\theta} = -1.98°C$, $\overline{S} = 34.53$) than that in the west ($\overline{\theta} = -2.06°C$, $\overline{S} = 34.46$). In the west, ISW is observed at depths from $\sim$350 to 660 m, between March and August. The coldest ISW ($-2.22°C$, 34.43) is observed at $\sim$350 m at PBM4 and PBM7 (Figures 5a and 5d). The temperature and salinity of ISW changes little from February to May. Between May and July, supercooled ISW, i.e., with temperature below the in situ freezing point, is observed at $\sim$360 m at PBM4, PBM6 and PBM7 (Figures 5a, 5c, and 5d). The presence of frazil ice
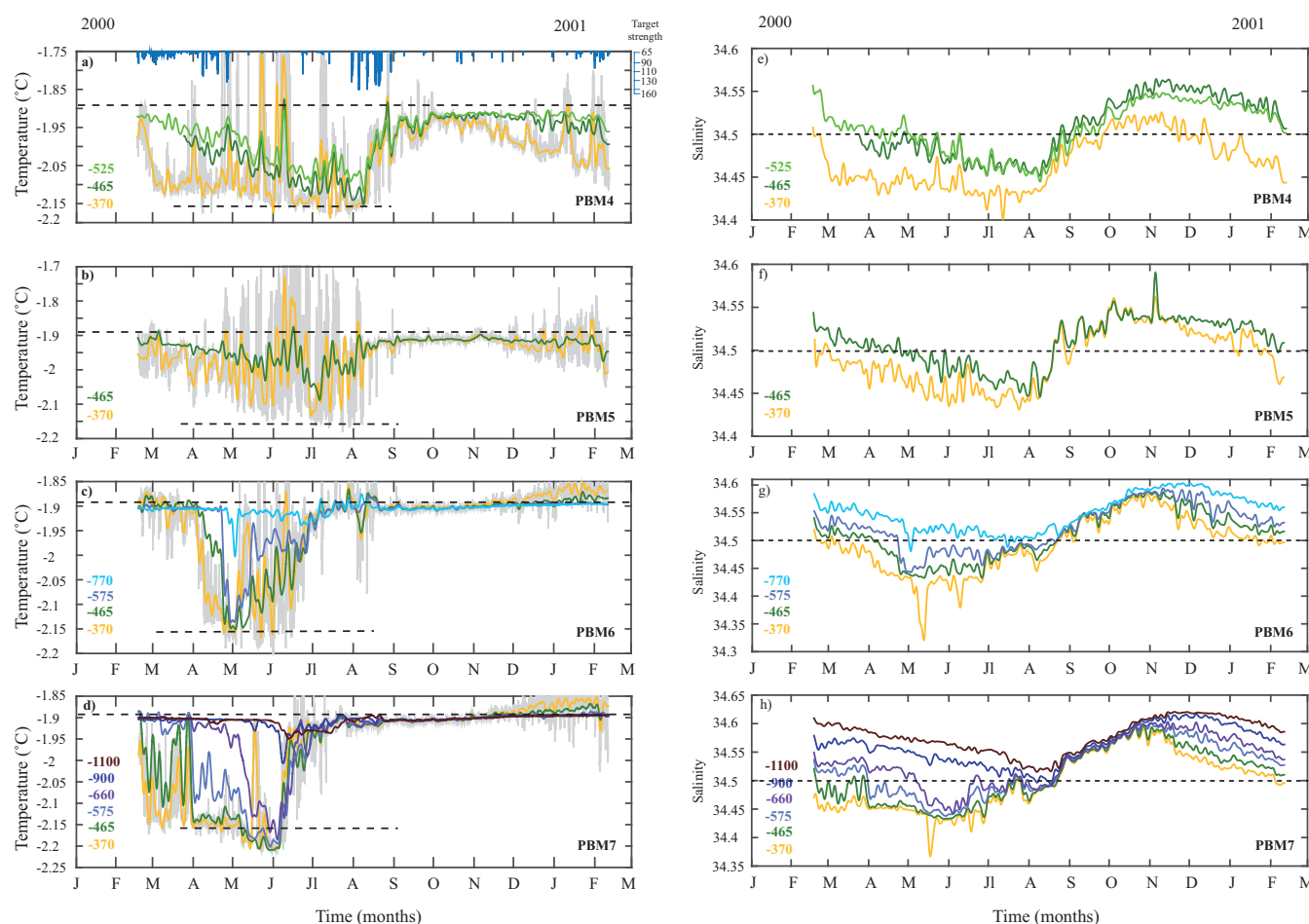
Figure 5. Time series of potential temperature at (a) PBM4, (b) PBM5, (c) PBM6, and (d) PBM7. The ADCP target strength signal for the bin number 15 (∼265 m below ocean surface) is shown in blue in Figure 5a. The times series have been filtered using a 48 h low-pass Butterworth filter. Each time series is color coded according to a nominal depth at which the measurements were sampled. The exact depth of the time series is shown in Table 1. The freezing temperature at the ocean surface is shown as a horizontal black dash line. The freezing temperature at 370 dbar is shown as a short horizontal black dash line at −2.15°C. The unfiltered time series of temperature is shown for the shallowest microCAT in grey. Note that the vertical axes have different temperature range. Time series of salinity at (e) PBM4, (f) PBM5, (g) PBM6, and (h) PBM7. As in Figures 5a–5d. The 34.5-isohaline is shown as a horizontal dashed line. Note that the vertical axes have different salinity range.

within the ISW plume has been observed at the Amery Ice Shelf front previously [*Penrose et al.*, 1994], as well as inferred from observations inside the western ice shelf cavity [*Herraiz-Borreguero et al.*, 2013; *Craven et al.*, 2014].

To test whether frazil ice is present in the outflow of supercooled ISW, we look for periods of large target strength signal in the ADCP at PBM4. Two periods are found to correlate with the temperature of the supercooled ISW, in April and August (Figure 5a, blue vertical lines). While the first event in April can also be explained by biological activity, this does not apply to the second event in August. Thus we interpret the latter as caused by the presence of frazil ice. This winter event shows the largest target strength event, which continues even after the supercooling event ends. The target strength signal shown in Figure 5a corresponds to a depth ∼100 m above the temperature sensor (∼260 m below the surface), suggesting supercooling conditions may occur at shallower depths as the ISW rises after leaving the ice shelf cavity and where the frazil ice is detected. This is possible as ISW occupies depths as shallow as the surface near the ice shelf front during the winter months (not shown).

The ISW plume thickens during the early winter to a minimum of 150 m at PBM4 (Figure 5a), and ∼300 m at PBM7 (Figure 5d). This thickening of the ISW plume at the ice shelf front follows the thickening of the ISW plume in the western side of the ice shelf cavity [*Herraiz-Borreguero et al.*, 2013] and the formation of frazil ice [*Craven et al.*, 2014].
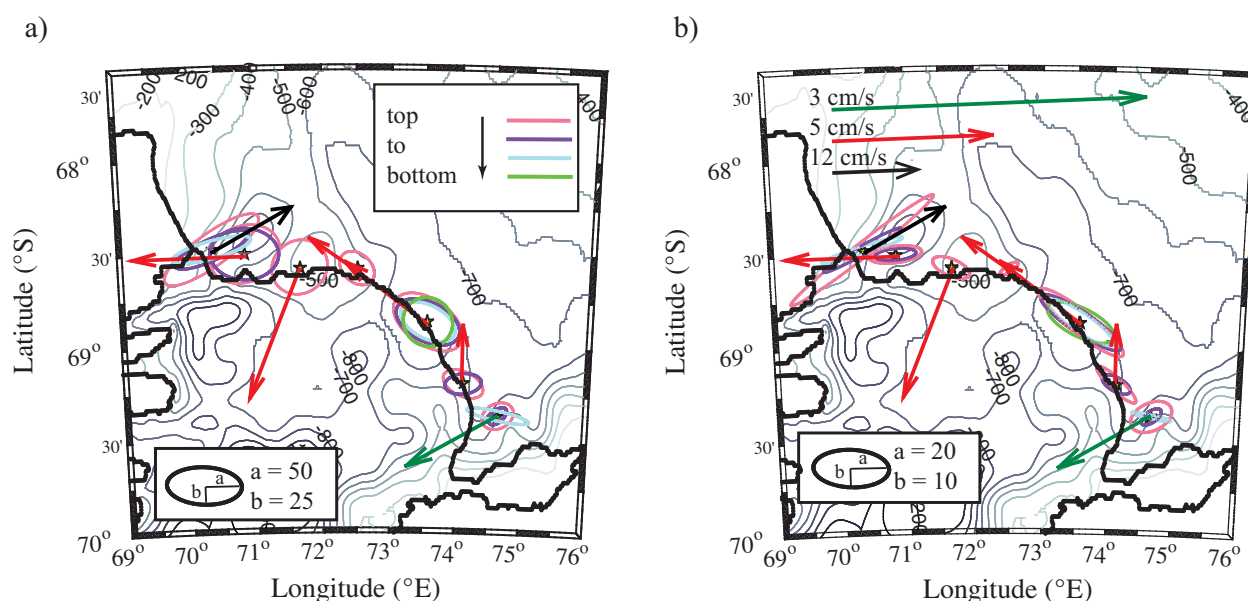
Figure 6. Maximum variance ellipses (cm^2 s^{-2}) of the (a) unfiltered and (b) 7 day low-pass Butterworth filtered velocity time series. Mean velocities ~465 dbar deep are shown in black, red, and green, depending on which scale the vectors were plotted against. Colors show the relative depth of the current meters within a single mooring. The location of each PBM is shown as a star. The ice shelf calving front and the coast is shown in black contours.

3.2. Ocean Circulation

The velocity components (u, v) have been rotated locally to directions of along/across the ice shelf front, here-after u-along and v-across. The velocity has been filtered using a 20 day low-pass filter and we will discuss these low-passed filtered currents in relation to the temperature and salinity time series in Figures 4 and 5.

The ocean circulation along the ice shelf calving front shows a complex interaction between the ocean current and changes in water column depth and the ice shelf front itself. The shipboard ADCP depicts a surface current that follows the ice shelf front westward (not shown) as described by *Nunes Vaz and Lennon* [1996]. However, the annual mean velocity vectors deviate slightly from this description (Figure 6), especially at the bottom currents in PBM1, PBM3, and PBM5 (Figures 7 and 8, right). Decomposition of the velocity into the axes of maximum (and minimum) variability shows ellipses with a small eccentricity, suggesting the presence of eddies and/or coastally trapped waves in the flow (Figure 6a). When we filter the time series, the eccentricity increases and the maximum variability of the velocity is more clearly seen aligning with the direction of the ice shelf front in most moorings. The moorings located near rapid changes in the bathymetry (PBM1, PBM4, and PBM5-7) deviate from this behavior and tend to follow the bathymetry contours (Figure 6b). In the case of PBM1, the maximum variability follows the bathymetry contours, except the bottom-most velocity, which is across the bathymetry

In the eastern moorings and from March to August, the upper u-along flow is westward in both PBM1 and PBM3, and eastward in PBM2 although the velocity is close to zero here (Figure 7). The deep u-along flow follows the upper layers, however the velocity is stronger in PBM2 than at the upper layers. During this same period, the v-across flow is predominantly inward in PBM1, with a stronger flow at the bottom, and outward in PBM2 and PBM3. It is during this period when mCDW is observed in this part of the ice shelf front (Figures 4a–4c), and DSW of temperature above the surface freezing point is observed at bottom layers (Figures 4d–4f).

The formation of sea ice influences the flow at the ice shelf front. Sea ice formation is marked by the onset of the salinity increase between July and August until salinity reaches a maximum in the eastern moorings (Figures 4d–4f). Both the u-along and v-across components of the velocity intensify at PBM1, and change to opposite directions until the end of the salinity increase (due to brine rejection) (Figures 7a and 7d). This period finishes with the outflow of ISW and the appearance of DSW of temperature slightly below the surface freezing point accompanied by an inflow at the deepest layers of PBM1-3 and in the upper layers at PBM1 and PBM3 (Figure 7). The change in the bathymetry contours toward the north at PBM2 likely explains the difference in the direction of the flow between PBM2 and PBM1 and PBM3.
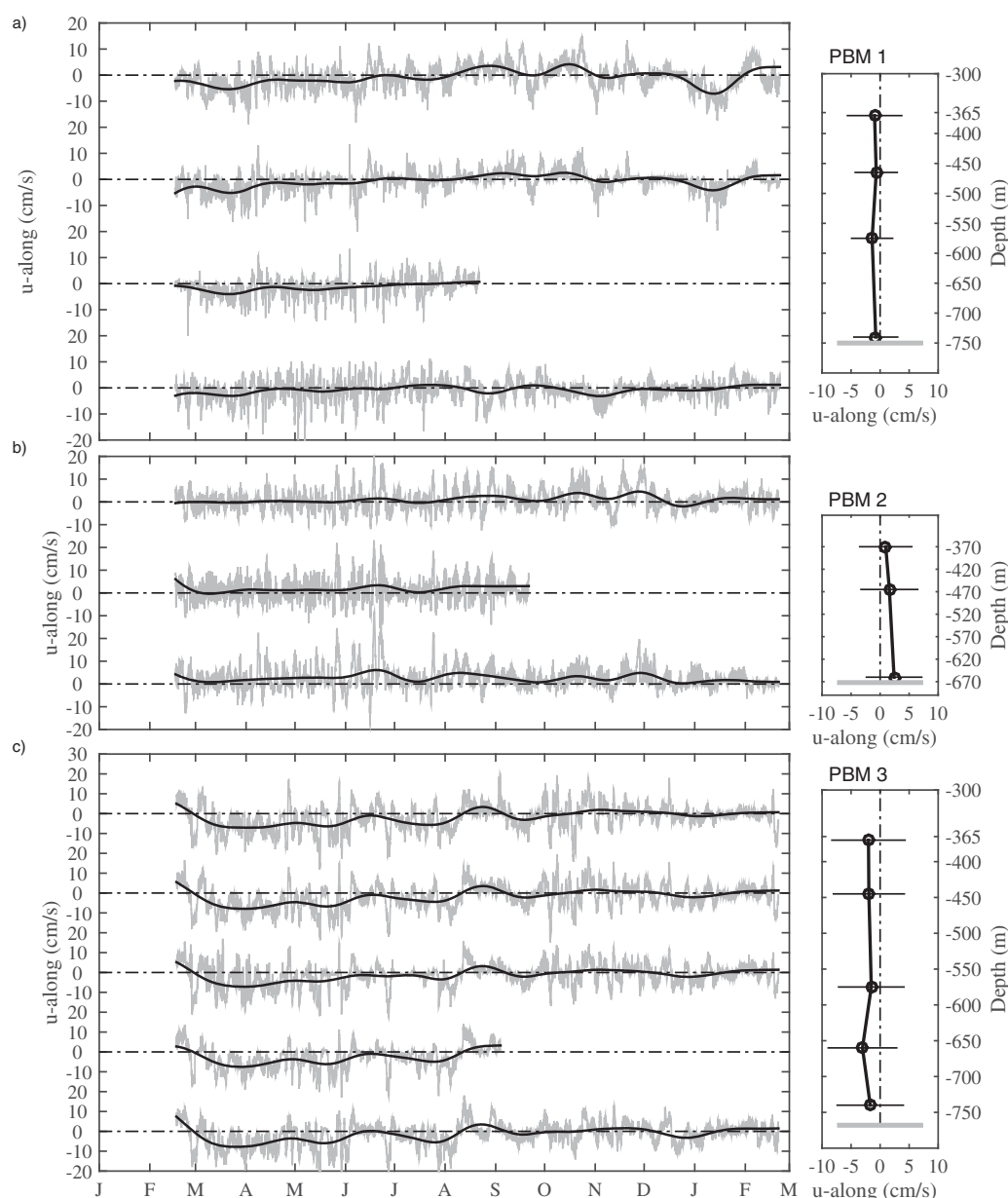
Figure 7. Time series of the along-shelf front velocity component in the eastern moorings (a) PBM1, (b) PBM2, and (c) PBM3. The velocity filtered by a 20 day low-pass Butterworth filter is shown overlaid in black. The right plots show the annual mean vertical profile and one standard deviation (horizontal bars); grey horizontal line shows the depth of the water column. Same as Figures 7a–7c for the across-shelf front velocity component in the eastern moorings (d) PBM1, (e) PBM2, and (f) PBM3.

The velocity in the western moorings is described as a westward current, dominated by the outflow or northward flow at all moorings except PBM5. The current at PBM7 is eastward, as the current needs to deflect as it encounters the coast. As in the eastern moorings, the formation of sea ice, and DSW at the Mackenzie polynya, influence the currents: (i) the onset of the salinity increase is observed in the velocity field as an increase in the variance and the energy field (section 4.2; Figure 10), and (ii) the current at PBM7 changes to southwestward when the water column is fully unstratified (Figures 5d, 5h, 8d, and 8h). It is also during this period that the current at PBM 6 is primarily southward (inflow).

The presence of the Mackenzie polynya on the western flank of the Amery Ice Shelf calving front plays a key role in the strength of the seasonal exchange between the open ocean and the ice shelf cavity. The seasonal formation of DSW in the Mackenzie polynya creates a pressure gradient along the shelf front, setting
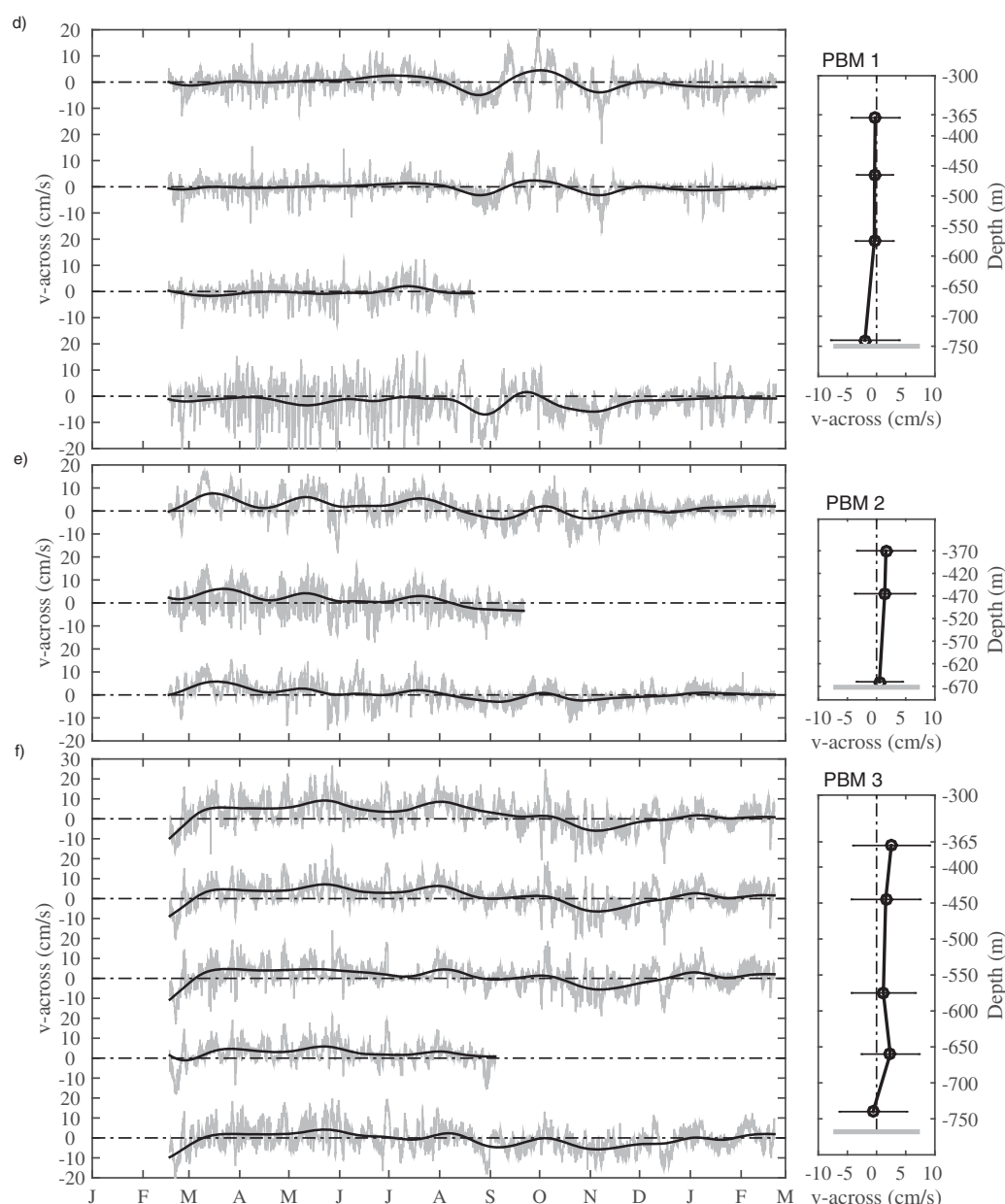
Figure 7. (continued)

up a geostrophic circulation, which connects the cyclonic gyre in Prydz Bay with the ocean circulation beneath the ice shelf. This pressure gradient (from east to west) is strongest in spring, between September and January (Figure 3d), and it implies an inflow in the eastern flank of the ice shelf front, which is observed in the velocity time series (Figure 7d–7f).

The high-frequency variability is discussed on the basis of rotary spectra and wavelet analyses. The rotary spectra per mooring are consistent in depth and only one depth is shown per mooring in Figure 9. Rotary spectra decompose complex time series ($z = u + iv$) into clockwise (S^-) and counter-clockwise (S^+) components that can be used to isolate features such as mesoscale eddies, inertial oscillations and some types of waves. There is a tendency for higher energy, concentrated in the 4–10 day bands, toward the west of the ice shelf front (Figure 9), with the exception of PBM5 where the current meter is located near the ocean bed. Across all moorings, high energy is concentrated in the 4–10 day frequency, where clockwise rotations (S^-, Figure 9, red line) are more frequent than counter-clockwise rotations (S^+, Figure 9, black line), with the exception of PBM3. These results suggest that mesoscale eddies dominate the high-frequency variability
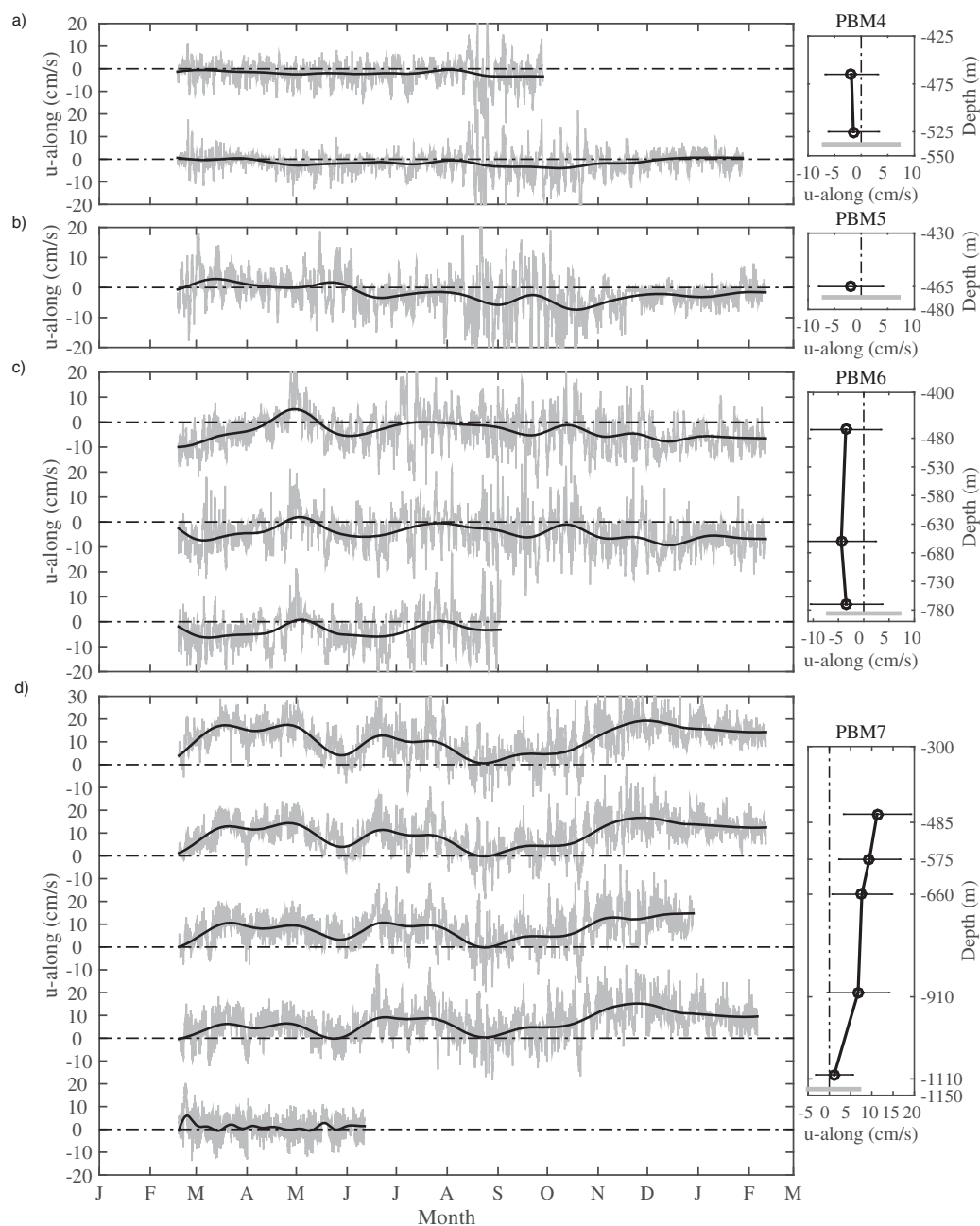
Figure 8. Time series of the along-shelf front velocity component in the western moorings (a) PBM4, (b) PBM5, (c) PBM6, and (d) PBM7. As in Figures 7a–7c. Same as Figures 8a–8d for the across-shelf front velocity component in the western moorings (e) PBM4, (f) PBM5, (g) PBM6, and (h) PBM7.

observed in the velocity across the ice shelf front. When there is an equal partition of energy between the S^- and S^+ components, the presence of rectilinear-like movements dominate. Such spectra are characteristic of the ocean currents near the ocean bed along the ice shelf front (not shown), and can be caused by topographic waves.

In order to illustrate the temporal variation of the spectrum, wavelet analysis was used, following *Grinsted et al.* [2004]. Wavelet analysis enables us to study nonstationary signals, in which the amplitudes of the frequency components of the signal are changing over time. Similar energy peaks are observed in both components of the velocity and thus, only the wavelet of the across-shelf component of the velocity is shown (Figure 10).
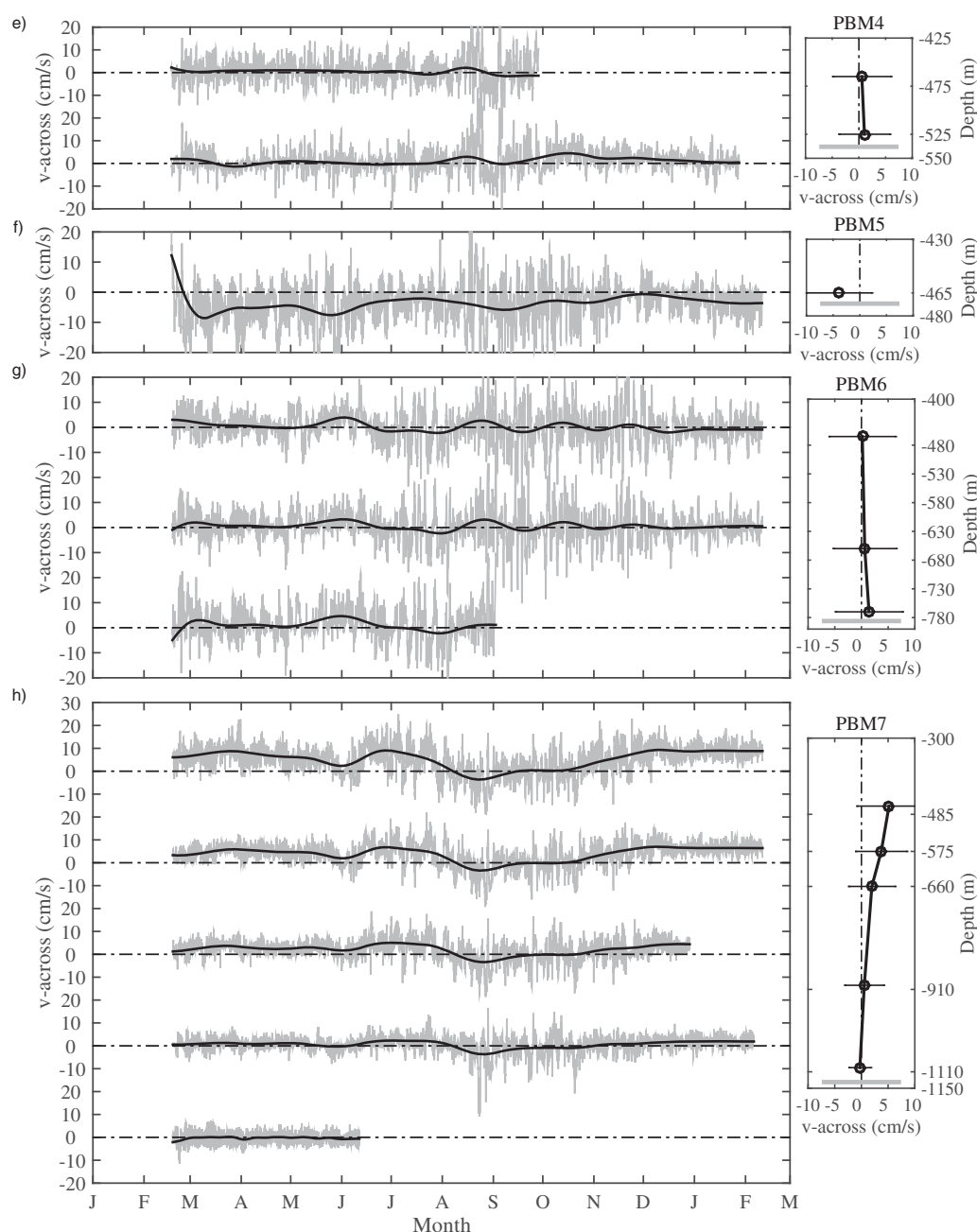
Figure 8. (continued)

On the eastern flank of the ice shelf front, the flow is highly energetic at a range of periods during the austral summer, followed by a low-energy period during the austral winter. This transition from high to low energy is supported by a change in the variance also from high to low variance (Figures 10a and 10b, top). Between March and the end of July, significant high-energy periods occur between 2 and 10 days (Figures 10a and 10b). The end of this high-energy period coincides with the onset of the gradual salinity increase due to sea ice formation (Figures 5a–5c).

On the western flank of the ice shelf front, the flow is highly energetic at a range of periods during the austral winter. The periods at which the energy field is significant range from 3 to 8 days (Figures 10c and 10d). The period of significant energy peaks occurs concurrently to the period when the water column is completely unstratified (Figures 5h, 10c, and 10d) due to deep convection driven by the Mackenzie polynya. Baroclinic eddies are the most likely explanation for this high-energy field and will be discussed further in
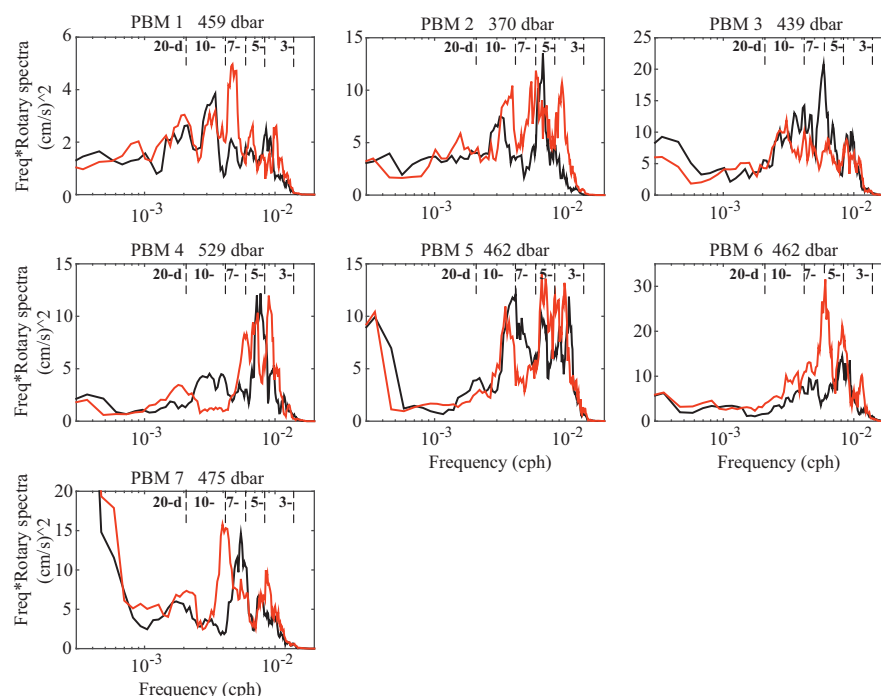
Figure 9. Variance-preserving rotary spectra of the velocity field (filtered to periods lower than 3 days) for PBM 1–7. The clockwise (S^-) and counter-clockwise (S^+) components of the spectra are shown in red and black lines, respectively. Note that the scales are different.

section 4.2. The significant energy peak at periods from 10 to 42 days occurs at various points of the year, which may be explained by barothopic Rossby waves [*Jensen et al.*, 2013].

4. Discussion

4.1. DSW Production and ISW Variability

The outflow of ISW limits the efficiency of the Mackenzie polynya to form DSW and affects the final DSW temperature and salinity. Generally, sea ice formation is followed by a gradual increase in ocean salinity due to brine rejection. In Prydz Bay, sea ice generally starts forming in March [*Massom et al.*, 2013]. However, a gradual increase in salinity occurs 2–4 months later in our moorings (Figures 4d–4f and 5e–5h). We contend that this delay in the salinity increase is due to the outflow of ISW on the western flank of the ice shelf front, where ISW mixes with the water column above during the formation of DSW by the Mackenzie polynya. Only when the ISW outflow weakens (or is diverted away from the mooring location), are the effects of brine in the densification of the water column through deep convection able to reach deeper into the water column (e.g., Figure 5h). This process results in a DSW with potential temperature ranging between −1.9 and −1.95°C, slightly below the surface freezing point of −1.89°C. The effect of ISW interacting with a polynya during DSW formation has also been observed in the Mertz Glacier polynya [*Williams et al.*, 2008] , resulting in a pause in the densification of the water column.

Two types of ISW have been identified beneath the Amery Ice Shelf as a result of different source waters and mixing processes beneath the shelf. In the northeastern flank of the ice shelf cavity, mCDW forms a fresher type of ISW (S ∼ 34.25) [*Herraiz-Borreguero et al.*, 2015]. However, the outflow of the fresher type of ISW is not captured by our mooring array, likely due to the recirculation of the ISW into the cavity as it mixes with the saltier type of ISW or outflow at shallower depths than the mooring instruments (<350 m). DSW is the source water for the saltier type of ISW (S > 34.4), which occupies most of the ice shelf cavity [*Herraiz-Borreguero et al.*, 2013, 2014]. This ISW is captured almost entirely by the western mooring array.

In θ-S space, the slope of a straight line describes the evolution of the mixing between glacial meltwater and the ambient ocean beneath the ice shelf to form ISW. This line is known as the melt-freeze line or Gade line [*Gade*, 1979]. To the first order, ISW properties depend on the θ-S of the source water mass that produced it, and are
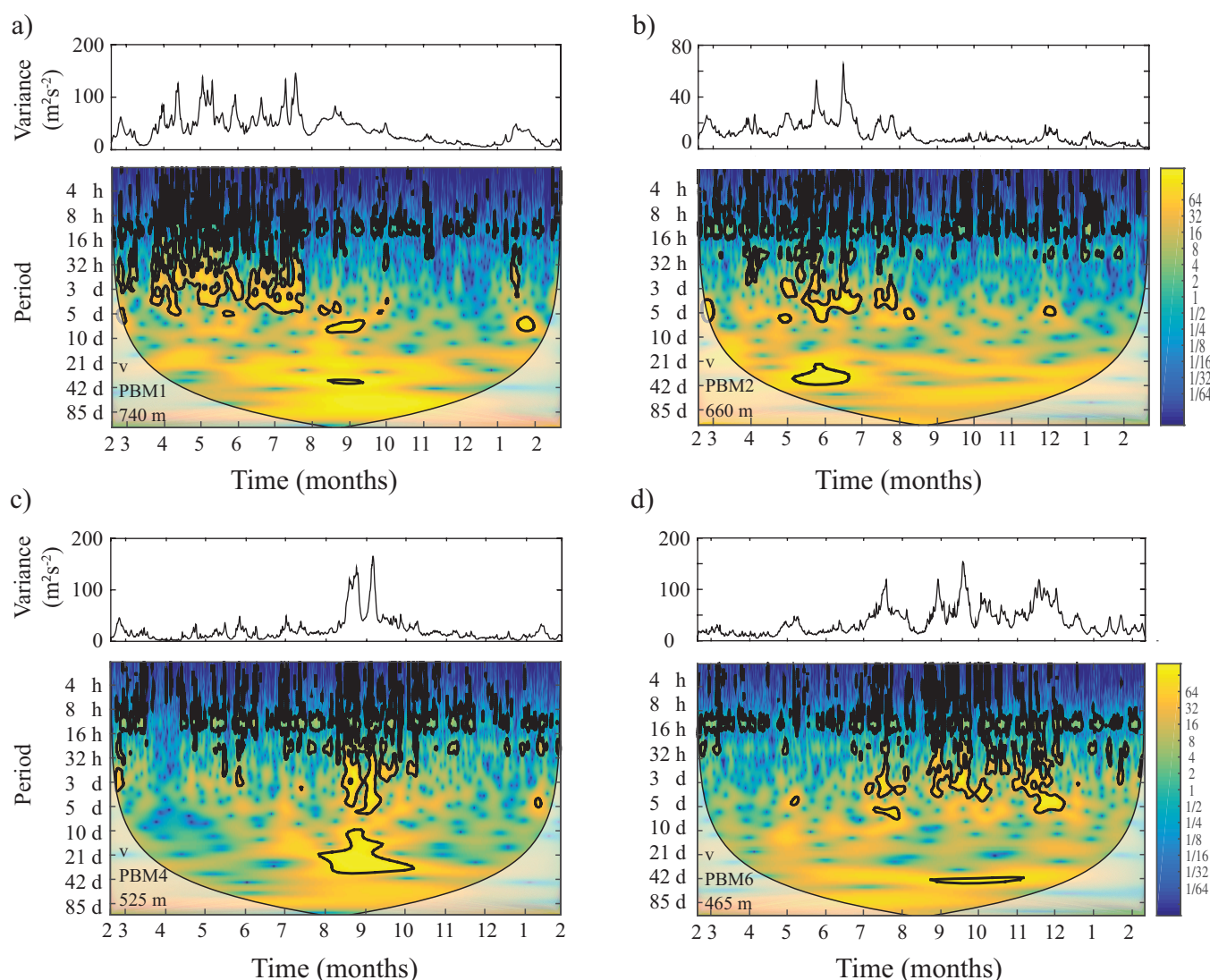
Figure 10. Continuous wavelet power spectrum of the across-shelf front at mooring (a) PBM1, (b) PBM2, (c) PBM4, and (d) PBM6. The 5% significant level against red noise is shown as black contours and the cone of influence where edge effects might distort the picture has been masked. The top plots show the variance expressed as the scale-averaged wavelet power [*Torrence and Compo*, 1998].

almost independent of entrainment and melt rates [*Nøst and Foldvik*, 1994]. Thus, further mixing of ISW with its source water has little or no effect on the $\Delta\theta/\Delta S$ relationship described by the Gade line. The mixing of ISW with the locally formed DSW follows the Gade line (Figure 11), suggesting that the source waters for the outflowing ISW is indeed the locally formed DSW. This is consistent with the results presented by previous observational [*Herraiz-Borreguero et al.*, 2013] and modeling [*Williams et al.*, 2001; *Galton-Fenzi et al.*, 2012] studies.

We have detected the presence of frazil ice in the ISW outflow during the austral winter. The presence of frazil ice within the western ISW plume has been previously observed at the AIS front during summer [*Penrose et al.*, 1994]. Frazil ice suspended within an ISW plume has also been observed in other regions around Antarctica, such as the Filchner Trough in the southern Weddell Sea [e.g. *Dieckmann et al.*, 1986] and McMurdo Sound in the Ross Sea [e.g. *Leonard et al.*, 2006]. We have shown that the presence of frazil ice suspended within the supercooled ISW using the ADCP target strength signal (Figure 5a), which outflows the Amery Ice Shelf cavity between May and August (Figures 5a–5d). This supercooled ISW (−2.22°C, 34.43) is observed at ∼350 m at PBM4 and PBM7 (Figures 5a and 5d). The degree of supercooling can give a rough indication of the minimum depth at which this ISW was formed. Assuming that this water was formed at an in situ freezing temperature of −2.22°C, and was transported adiabatically to 350 dbar, then it must have originated
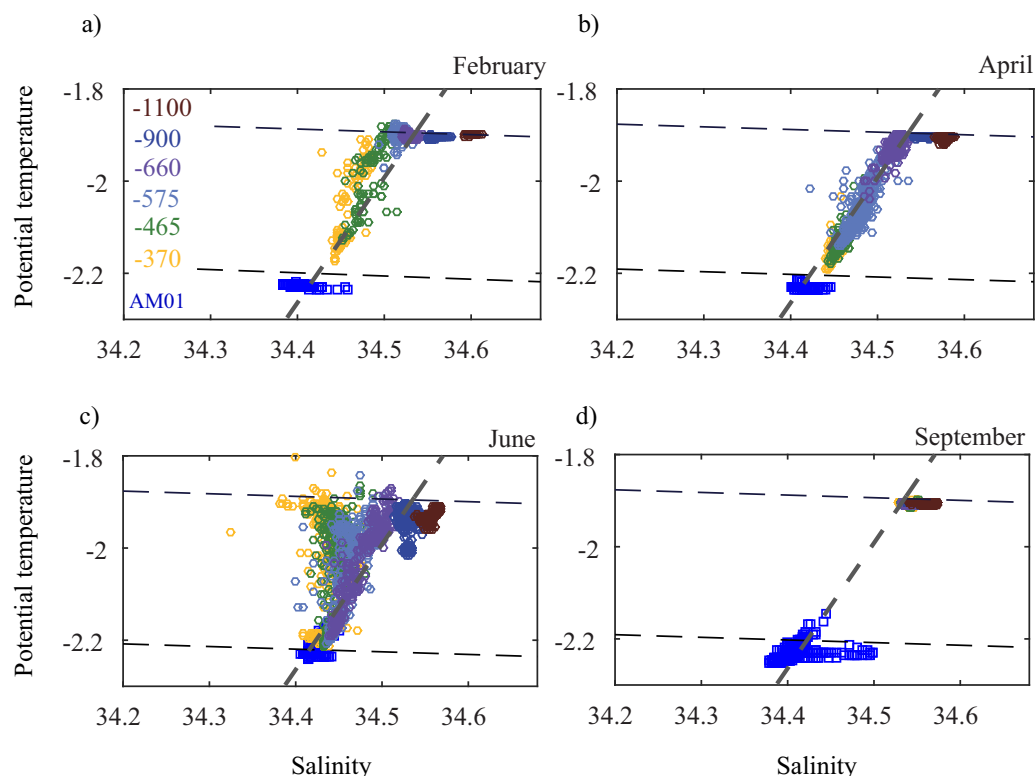
Figure 11. Seasonal temperature and salinity diagrams at PBM7 during (a) February, (b) April, (c) June, and (d) September in 2001, together with data measured at borehole AM01 in 2002 in blue squares. Color coding follows the same coding as Figure 5. Two almost horizontal dashed lines show the temperature at the surface ($\theta \sim -1.89°C$) and 370 dbar ($\theta \sim -2.2$) freezing point. The grey dashed line shows the melt-freeze line or Gade line.

from a depth of at least 430 dbar (at P = 350 dbar, S = 34.43, $T_f = -2.22°C$). This depth is found at the ice shelf base in borehole AM01, about 100 km south of the calving front (Figure 1). The θ-S properties of the ISW at AM01 and the supercooled ISW outflowing the Amery Ice Shelf cavity are identical (Figure 11c).

The Mackenzie polynya is the primary source of DSW to the ice shelf cavity. So far we have focused on DSW formation within the western flank of the calving front, however, DSW is also observed in the deepest layers (>600 m) in the east, in particular at PBM3. Here DSW with temperature between the surface freezing temperature and $-1.8°C$ (with no significant change in salinity) is observed from March to October (Figures 4c and 4f). From October onward, DSW temperatures drop below the surface freezing point and the salinity gradually increases until ~December (Figure 5c). This low temperature results from the mixing between ISW and locally formed DSW within the Mackenzie polynya (Figure 11), suggesting that the DSW observed in the east is likely supplied primarily from the Mackenzie polynya. The Barrier polynya, in the northeast of Prydz Bay, likely supplies additional DSW to Prydz Bay. However, the densest DSW of the Barrier polynya is blocked from traveling south by the Four Ladies Bank, and DSW < 300 m is likely to mix across and flow toward the Amery Ice Shelf front (G. D. Williams, personal communication, 2016).

4.2. Ocean Current Variability and Deep Convection Processes

In some ice shelf cavities, tidal forcing is a significant source of energy for mixing, capable of altering the transfer of heat and salt in the ice shelf cavity, and consequently the mean thermohaline circulation [e.g., *MacAyeal*, 1984; *Makinson and Nicholls*, 1999]. Beneath the Amery Ice Shelf, tidal forcing and the induced vertical mixing are found to be too weak to destroy the stratification [*Hemer et al.*, 2006], in contrast to other large ice shelves like, e.g., the Ronne-Filchner where tidal mixing is known to be significant [e.g., *Makinson et al.*, 2011]. For this reason, we focus on periods longer than 2 days.

The flow along the ice shelf front is best described as an eddy-rich flow, superimposed in the large-scale circulation. As previously shown, the decomposition of the velocity into axes of maximum (and minimum)

variability shows ellipses with a small eccentricity, suggesting the presence of eddies and/or coastally trapped waves in the flow (Figure 6a). The frequency and wavelet analyses also show that most of the energy is found at the frequency ranges occupied by eddies and coastally trapped waves (Figures 10c and 10d). Our results are consistent with summertime hydrographic/ADCP observations that revealed an eddy-rich flow field along the Amery Ice Shelf calving front affecting the whole water column [*Shanahan*, 2002]. In addition, the wavelet analysis allows us to distinguish any seasonality and spatial differences in the energy field between the east and west flanks of the ice shelf front, and in particular, the role of the McKenzie polynya.

While in the east, the variability in the flow is likely to be dominated by the interaction of the coastal current with the ice shelf front, in the west the variability in the flow is dominated by the deep convection driven by the McKenzie polynya. In regional scales, conservation of potential vorticity causes the flow to follow contours of constant depth. Thus, the ice shelf constitutes a barrier for the flow to enter the ice shelf cavity [*Grosfeld et al.*, 1997]. In the east, the high-energy period is likely a reflection of the coastal current response to the ice shelf front, and any seasonal change in the location of the current with respect to the ice shelf front. A recent modeling study suggests that the Prydz Bay gyre reduces its intensity during the austral winter [*Galton-Fenzi*, 2009] and in fact, its southern edge migrates north [see *Galton-Fenzi*, 2009, Figure 6.14]. In contrast, in the west, the most energetic motions occur between July and November when katabatic winds remove sea ice from the area as it forms, keeping the temperatures of the ocean surface around the freezing point ($\sim-1.89°C$). Large oceanic heat loss within the polynya results in deep convection and deep mixed layer of up to 1100 m thick at the location of PBM7, with temperature near-surface freezing point and salinity larger than 34.60 (Figures 5d and 5h, respectively).

Vertical buoyancy transfer by upright convection can give way to slantwise transfer by baroclinic instabilities laterally exchanging fluid with the surroundings of the convection area [*Marshall and Schott*, 1999]. The mixed patches of fluid move away from the convection area via mesoscale eddies that form once the baroclinic instabilities dominate the convection process. Baroclinic instabilities/eddies have been claimed to be responsible for the inflow of DSW into ice shelf cavities at periods of 5–7 days [e.g., *Årthun et al.*, 2013; *Herraiz-Borreguero et al.*, 2013]. These eddies are clearly captured by the wavelet analyses of the western moorings at periods between 3 and 8 days (Figures 10c and 10d). The period of significant energy peaks (between July and November) occurs concurrently with the period when the water column is completely unstratified (e.g., Figure 5h). Mooring PBM7, in contrast to the other western moorings, shows no significant peak of energy during active convection in the upper layers but it is observed at the deepest current meter (not shown). PBM3 is the only eastern mooring that shows a similar winter energy peak signal as the western moorings at depths shallower than 500 m, highlighting the far-reaching influence of the Mackenzie polynya.

4.3. Basal Melt Rates Estimates

Now that we have identified the main processes and water masses interacting with the Amery Ice Shelf, we can calculate the heat flux into the ice shelf cavity and consequently, estimate the basal melt rate.

The ocean circulation below the Amery Ice Shelf is composed of two well-defined modes of circulation [*Herraiz-Borreguero et al.*, 2015]. In the western subice shelf cavity, the first mode comprises the ice-pump circulation through the inflow of DSW, basal melt in the deepest part of the grounding line and, the formation of ISW [*Galton-Fenzi et al.*, 2012; *Herraiz-Borreguero et al.*, 2013] and a marine ice layer [*Fricker et al.*, 2001]. In the eastern subice shelf cavity, the second mode comprises the inflow of mCDW at intermediate depths and the formation of a fresher type of ISW [*Herraiz-Borreguero et al.*, 2015]. This mode affects the outer eastern flank of the Amery Ice Shelf and works in conjunction with the dominant DSW-mode (this one taking over when the inflow of mCDW is exhausted). The third mode depicted at the calving front occurs along the ice shelf front. Note that this depiction of the sub ice shelf circulation does not exclude zonal flows, but highlights the zonal contrast in the interaction of the ocean with the Amery Ice Shelf, which we also observed along the ice shelf front. This regional pattern in basal melt and freezing is in agreement with satellite-based studies [*Wen et al.*, 2010], and modeling studies [*Williams et al.*, 2001; *Galton-Fenzi et al.*, 2012]. However, the inflow of warm mCDW has not been realistically simulated yet.

We begin by estimating the transport of the different water masses (DSW, ISW and mCDW) through the array of moorings. We calculate these transports by multiplying the across-shelf component of current velocity by the area of a vertical section centered around each of the current meters on the PBM moorings. The typical width of these sections is 34 km, and the typical height is 100 m. The choice of area is likely to introduce

Table 2. Summary of the Most Recent Estimates of Net Basal Melt Beneath the Amery Ice Shelf

Study	Net Basal Melt (m yr^{-1})	Net Basal Mass Loss (Gt yr^{-1})
This study + *Herraiz-Borreguero et al.* [2015][a,b]	1.0 ± 0.4	57.4 ± 25.3
Depoorter et al. [2013][c]	0.65 ± 0.35	39 ± 21
Rignot et al. [2013][c]	0.58 ± 0.4	35.5 ± 22
Galton-Fenzi et al. [2012][d]	0.74	45.6
Yu et al. [2010][c]	0.5 ± 0.12	27 ± 7
Wen et al. [2010][c]	0.84 ± 0.12	46.4 ± 6.9

[a]Oceanographic study.
[b]Has been adjusted to give a net basal melt estimate in m/yr over the whole ice shelf area.
[c]Glaciological study.
[d]Modeling study.

some errors in the transport calculations given the eddy/jet-like structure of the horizontal velocity at the ice shelf front [*Shanahan*, 2002].

The presence of eddies and topographic waves can also impact our transport estimates if they are not well resolved. Overall the strength and mean life span of eddies that enter the cavity is currently unknown. We present transport values of the water masses estimated with a 7 day low-pass Butterworth filter, to minimize the effect of these features, as most of the energy and variability of the horizontal velocities occupy periods lower than 7 days (Figure 9).

The observations of temperature and salinity were used to estimate the net heat and freshwater exchange between the ocean cavity beneath the Amery Ice Shelf and the ocean. We use this transport value to estimate the net basal melt rate from heat exchange (m_H) and from freshwater exchange (m_{FW}) as follows:

$$m_H = F\rho_{sw}(\theta_{in}-\theta_{out})c_{sw}\ [L+c_{sw}\ (\theta_{out}-\theta_f)+c_i(\theta_f-\theta_{ice})]^{-1} \tag{1}$$

$$m_{FW} = F\rho_{sw}\left(\frac{S_{in}-S_{out}}{S_{out}}\right) \tag{2}$$

where F is the flux of DSW into the ice shelf cavity (0.52 ± 0.38 Sv; 1 Sv = 10^6 m^3 s^{-1}), ρ_{sw} is ocean density (1027 kg m^{-3}), c_{sw} is the ocean heat capacity (4000 J kg^{-1} °C^{-1}), θ_{in} and S_{in} are the temperature and salinity of the DSW (−1.92°C and 34.53, respectively), θ_{out} and S_{out} are the temperature and salinity of the ISW (−2.09°C and 34.45, respectively), c_i is the ice heat capacity (2090 J kg^{-1} °C^{-1}), θ_f is the freezing temperature (at 800 dbar and a salinity of 34.53), θ_{ice} is the temperature of the basal ice (here we use the temperature of the glacial ice, −15°C, measured from a thermistor cable at AM01 [*Herraiz-Borreguero et al.*, 2013], and L is the latent heat of ice (334,000 J kg^{-1}). The θ and S of the DSW were chosen to be representative of the values observed within the ice shelf cavity, at boreholes AM06 and AM03 (Figure 1), which are 160–210 km into the ice shelf cavity, respectively. These values represent the DSW properties within the DSW path in the cavity toward the deep grounding line. In the case of ISW, we have chosen the mean values measured for an ISW with temperature lower than −2°C. Below this temperature, ISW properties show low variability (e.g., Figure 5a, orange line) and we believe this value represents the purest ISW outflowing the ocean cavity and minimizes the effect of mixing driven by the polynya with the ambient water.

An inflow of DSW of 0.52 ± 0.38 Sv yields a net basal melt of 33.5 ± 24.4 Gt yr^{-1}. If this was evenly distributed under the ice shelf area (60,000 km^2) and using the density of ice (920 kg m^{-3}), it would amount to an average basal melt rate of 0.6 ± 0.4 m ice yr^{-1}. Using the salt budget equation, the inflow of DSW yields a net basal melt of 39.1 ± 28.6 Gt yr^{-1} (equivalent to 0.7 ± 0.5 m ice yr^{-1}). These two estimates are consistent within the uncertainty. If we add the basal melt estimate driven by mCDW (based on heat) of 23.9 ± 6.52 Gt yr^{-1}, over a limited area near the ice shelf front [*Herraiz-Borreguero et al.*, 2015], the net basal melt estimate beneath the Amery Ice Shelf adds up to 57.4 ± 25.3 Gt yr^{-1}.

Several studies have provided net basal melt estimates for the Amery Ice Shelf (Table 2) using glaciological, oceanographic, and modeling approaches. *Wong et al.* [1998] provided net basal melt estimates using oceanographic observations in Prydz Bay, however, the data used for their study have been deemed biased due to instrumental malfunction [*Bindoff et al.*, 2003], and it is not reported in Table 2. Glaciological studies (Table 2) provide a wide range of net basal melt estimates of 27 ± 7 to 46.5 ± 6.9 Gt yr^{-1}, with the most recent regional ocean model estimate (45.6 Gt yr^{-1}) [*Galton-Fenzi et al.*, 2012] lying well within the uncertainty of the glaciological estimates. Our ice shelf basal melt estimates are within the largest estimates provided previously by several studies.

Large inter-annual variability in mCDW and DSW inflows may explain the large basal estimate we have estimated. Heat content associated with mCDW inflows observed ~80 km inward from the ice shelf front showed large inter-annual variability in the ocean heat content, e.g., +40% in 2001–2002 compared to heat

content in 2004–2005 [*Herraiz-Borreguero et al.*, 2015]. Together with our higher values for basal melting compared to previous studies suggests stronger inter-annual variability than previously acknowledged.

5. Conclusions

The two main water masses that drive basal melt under the Antarctic ice shelves are Dense Shelf Water (DSW) and modified Circumpolar Deep Water (mCDW), yet it remains unclear what controls the inflow of these waters into ice shelves cavities.

Here we have shown that for the Amery Ice Shelf, the Mackenzie polynya controls the seasonal exchange of dense waters into the ice shelf cavity, through: (1) setting up a horizontal density gradient between September and January, which favors inflow on the eastern flank of the ice shelf front, and (2) by forming baroclinic instabilities (during deep convection), which carry DSW into the cavity. The ice shelf is a dynamical barrier for ocean currents to enter the ice shelf cavity. MCDW inflow is likely controlled by how the eastern coastal current adjusts to a sudden change in water column due to the presence of the ice shelf front.

The contribution of the Amery Ice Shelf-ocean interaction to the formation of Antarctic Bottom Water has been a motive for discussion for over a decade. Our results reveal the role of the ISW in controlling the formation rate and thermohaline properties of DSW. The ISW outflow, thus, may influence the contribution of DSW to Cape Darnley Bottom Water [*Ohshima et al.*, 2013], and consequently, its inter-annual variability [*Couldrey et al.*, 2013].

In summary, we provide a comprehensive estimate of net basal melt (57.4 ± 25.3 Gt yr^{-1}) of the Amery Ice Shelf based on oceanographic measurements. Our estimate lies above previous basal melt estimates, based on model and glaciological results which ranged between 27 ± 7 and 46.5 ± 6.9 Gt yr^{-1}. The observed inter-annual variability in mCDW heat content beneath the Amery Ice Shelf together with our higher values for basal melting compared to previous studies suggest stronger inter-annual variability in the ocean forcing than previously acknowledged.

References

Allison, I. (1979), The mass budget of the Lambert Glacier drainage basin, Antarctica, *J. Glaciol.*, *22*(87), 223–235.

Årthun, M., P. R. Holland, K. W. Nicholls, and D. L. Feltham (2013), Eddy–Driven exchange between the open ocean and a Sub–Ice Shelf Cavity, *J. Phys. Oceanogr.*, *43*(11), 2372–2387.

Bamber, J. L., and W. P. Aspinall (2013), An expert judgement assessment of future sea level rise from the ice sheets, *Nat. Clim. Change*, *3*(4), 424–427, doi:10.1038/nclimate1778.

Bindoff, N. L., A. Forbes, and A. P. S. Wong (2003), Data on bottom water in Prydz Bay, Antarctica, revised, Eos Trans., *AGU*, *84*(21), 200–200, doi:10.1029/2003EO210005.

Church, J. A., et al. (2013), Sea level change, in *Climate Change 2013: The Physical Science Basis. Contribution of Working Group I to the Fifth Assessment Report of the Intergovernmental Panel on Climate Change*, edited by T. F. Stocker et al., pp. 1137–1216, Cambridge Univ. Press, Cambridge, U. K.

Clough, J. W., and B. L. Hansen (1979), The Ross Ice Shelf Project, *Science*, *203*(4379), 433–434, doi:10.1126/science.203.4379.433.

Couldrey, M. P., L. Jullion, A. C. Naveira Garabato, C. Rye, L. Herráiz-Borreguero, P. J. Brown, M. P. Meredith, and K. L. Speer (2013), Remotely induced warming of Antarctic Bottom Water in the eastern Weddell gyre, *Geophys. Res. Lett.*, *40*, 2755–2760, doi:10.1002/grl.50526.

Craven, M., I. Allison, H. A. Fricker, and R. Warner (2009), Properties of a marine ice layer under the Amery Ice Shelf, *J. Glaciol.*, *55*(192), 717–728.

Craven, M., R. C. Warner, B. K. Galton-Fenzi, L. Herraiz-Borreguero, S. I. Vogel, and I. Allison (2014), Platelet ice attachment to instrument strings beneath the Amery Ice Shelf, East Antarctica, *J. Glaciol.*, *60*(220), 383–393.

Depoorter, M. A., J. L. Bamber, J. A. Griggs, J. T. M. Lenaerts, S. R. M. Ligtenberg, M. R. van den Broeke, G. Moholdt (2013), Calving fluxes and basal melt rates of Antarctic ice shelves, *Nature*, *502*(7469), 89–92.

Dieckmann, G., G. Rohardt, H. H. Hellmer, and J. Kipfstuhl (1986), The occurrence of ice platelets at 250 m depth near the Filchner Ice Shelf and its significance for sea ice biology, *Deep Sea Res., Part I*, *33*, 141–148.

Dutrieux, P., J. De Rydt, A. Jenkins, P. R. Holland, H. K. Ha, S. H. Lee, E. J. Steig, Q. Ding, E. P. Abrahamsen, and M. Schröder (2014), Strong sensitivity of pine island ice–shelf melting to climatic variability, *Science*, *343*(6167), 174–178.

Foldvik, A., and T. Kvinge (1974), Conditional instability of seawater at the freezing point, *Deep Sea Res. Oceanogr. Abstr.*, *21*, 169–174.

Foldvik, A., et al. (2001), Current measurements near Ronne Ice Shelf: Implications for circulation and melting, *J. Geophys. Res.*, *106*(C3), 4463–4477.

Foster, T. D. (1983), The temperature and salinity fine-structure of the ocean under the Ross Ice Shelf, *J. Geophys. Res.*, *88*(C4), 2556–2564.

Fricker, H. A., S. Popov, I. Allison, and N. Young (2001), Distribution of marine ice beneath the Amery Ice Shelf, *Geophys. Res. Lett.*, *28*(11), 2241–2244.

Gade, H. G. (1979), Melting of ice in sea water: A primitive model with application to the Antarctic ice shelf and icebergs, *J. Phys. Oceanogr.*, *9*, 189–198, doi:10.1175/1520-0485(1979).

Galton-Fenzi, B. K. (2009), Modelling ice-shelf/ocean interaction, PhD dissertation, Univ. of Tasmania, Hobart, Australia.

Galton-Fenzi, B. K., J. R. Hunter, R. Coleman, S. J. Marsland, and R. C. Warner (2012), Modeling the basal melting and marine ice accretion of the Amery Ice Shelf, *J. Geophys. Res.*, *117*, C09031, doi:10.1029/2012JC008214.

Grinsted, A., J. C. Moore, and S. Jevrejeva (2004), Application of the cross wavelet transform and wavelet coherence to geophysical time series, *Nonlinear Processes Geophys.*, *11*, 561–566, doi:10.5194/npg-11-561-2004.

Grosfeld, K., R. Gerdes, and J. Determann (1997), Thermohaline circulation and interaction between ice shelf cavities and the adjacent open ocean, *J. Geophys. Res.*, *102*(C7), 15,595–15,610.

Hemer, M. A., J. R. Hunter, and R. Coleman (2006), Barotropic tides beneath the Amery Ice Shelf, *J. Geophys. Res.*, *111*, C11008, doi:10.1029/2006JC003622.

Herraiz-Borreguero, L., I. Allison, M. Craven, K. W. Nicholls, and M. A. Rosenberg (2013), Ice shelf/ocean interactions under the Amery Ice Shelf: Seasonal variability and its effect on marine ice formation, *J. Geophys. Res. Oceans*, *118*, 7117–7131, doi:10.1002/2013JC009158.

Herraiz-Borreguero, L., R. Coleman, I. Allison, S. R. Rintoul, M. Craven, and G. D. Williams (2015), Circulation of modified Circumpolar Deep Water and basal melt beneath the Amery Ice Shelf, East Antarctica, *J. Geophys. Res. Oceans*, *120*, 3098–3112, doi:10.1002/2015JC010697.

Jacobs, S. S., A. L. Gordon, and J. L. Ardai Jr. (1979), Circulation and melting beneath the Ross Ice Shelf, *Science*, *203*, 439–443, doi:10.1126/science.203.4379.439.

Jensen, M. F., I. Fer, and E. Darelius (2013), Low frequency variability on the continental slope of the southern Weddell Sea, *J. Geophys. Res. Oceans*, *118*, 4256–4272, doi:10.1002/jgrc.20309.

Joughin, I., B. E. Smith, and B. Medley (2014), Marine ice sheet collapse potentially under way for the Thwaites Glacier Basin, West Antarctica, *Science*, *344*(6185), 735–738.

Khazendar, A., J. L. Tison, B. Stenni, M. Dini, and A. Bondesan (2001), Significant marine ice accumulation in the ablation zone beneath an Antarctic ice shelf, *J. Glaciol.*, *47*, 359–368, doi:10.3189/172756501781832160.

Khazendar, A., E. Rignot, and E. Larour (2009), Roles of marine ice, rheology, and fracture in the flow and stability of the Brunt/Stancomb-Wills Ice Shelf, *J. Geophys. Res.*, *114*, F04007, doi:10.1029/2008JF001124.

LeBlond, P. H., and L. A. Mysak (1978), *Waves in the Ocean, Elsevier Oceanogr. Ser.*, 20, 602 pp.

Leonard, G. H., C. R. Purdie, P. J. Langhorne, T. G. Haskell, M. J. M. Williams, and R. D. Frew (2006), Observations of platelet ice growth and oceanographic conditions during the winter of 2003 in McMurdo Sound, Antarctica, *J. Geophys. Res.*, *111*, C04012, doi:10.1029/2005JC002952.

Leffanue, H., and M. Craven (2004), Circulation and water masses from current meter and T/S measurements at the Amery Ice Shelf, Tech. Rep. 15, Forum for research into Ice shelf-ocean interactions (FRISP).

MacAyeal, D. R. (1984), Thermohaline circulation below the Ross Ice Shelf: A consequence of tidally induced vertical mixing and basal melting, *J. Geophys. Res.*, *89*(C1), 597–606.

Makinson, K., and K. W. Nicholls (1999), Modeling tidal currents beneath Filchner-Ronne Ice Shelf and on the adjacent continental shelf: Their effect on mixing and transport, *J. Geophys. Res.*, *104*(C6) 13,449–13,465, doi:10.1029/1999JC900008.

Makinson, K., P. R. Holland, A. Jenkins, K. W. Nicholls, and D. M. Holland (2011), Influence of tides on melting and freezing beneath Filchner-Ronne Ice Shelf, Antarctica, *Geophys. Res. Lett.*, *38*, L06601, doi:10.1029/2010GL046462.

Marshall, J., and F. Schott (1999), Open-ocean convection: Observations, theory, and models, *Rev. Geophys.*, *37*(1), 1–64.

Massom, R., P. Reid, S. Stammerjohn, B. Raymond, A. Fraser, and S. Ushio (2013), Change and variability in East Antarctic sea ice seasonality, 1979/80–2009/10, *PLoS ONE*, *8*(5), e64756, doi:10.1371/journal.pone.0064756.

Morgan, V. I. (1972), Oxygen isotope evidence for bottom freezing on the Amery Ice Shelf, *Nature*, *238*(5364), 393–394.

Nicholls, K. W., and A. Jenkins (1993), Temperature and salinity beneath Ronne Ice Shelf, Antarctica, *J. Geophys. Res.*, *98*, 22,553–22,568, doi:10.1029/93JC02601.

Nøst, O., and A. Foldvik (1994), A model of ice shelf–ocean interaction with application to the Filcher–Ronne and Ross Ice Shelves, *J. Geophys. Res.*, *99*(C7), 14,243–14,254

Nunes Vaz, R. A., and G. W. Lennon (1996), Physical oceanography of the Prydz Bay region of Antarctic waters, *Deep Sea Res., Part I*, *43*, 603–641.

Ohshima, K. I., et al. (2013), Antarctic Bottom Water production by intense sea–ice formation in the Cape Darnley Polynya, *Nat. Geosci.*, *6*, 235–240, doi:10.1038/ngeo1738.

Penrose, J. D., M. Conde, and T. J. Pauly (1994), Acoustic detection of ice crystals in Antarctic waters, *J. Geophys. Res.*, *99*(C6), 12,373–12,380.

Pritchard, H. D., S. R. M. Ligtenberg, H. A. Fricker, D. G. Vaughan, M. R. Van den Broeke, and L. Padman (2012), Antarctic ice-sheet loss driven by basal melting of ice shelves, *Nature*, *484*(7395), 502–505.

Rignot, E., S. Jacobs, J. Mouginot, and B. Scheuchl (2013), Ice-shelf melting around Antarctica, *Science*, *341*(6143), 266–270.

Shanahan, M. J. (2002), Ocean Interactions with the Amery Ice Shelf from ocean measurements, BSc thesis, Univ. of Tasmania, Hobart, Australia.

Smith, N. R., D. Zhaoqian, K. R. Kerry, and S. Wright (1984), Water masses and circulation in the region of Prydz Bay, Antarctica, *Deep Sea Res., Part I*, *31*(9), 1121–1147.

Tamura, T., K. I. Ohshima, and S. Nihashi (2008), Mapping of sea ice production for Antarctic coastal polynyas, *Geophys. Res. Lett.*, *35*, L07606, doi:10.1029/2007GL032903.

Torrence, C., and G. P. Compo (1998), A practical guide to wavelet analysis, *Bull. Am. Meteorol. Soc.*, *79*(1), 61–78.

Van den Broeke, M. R, and N. P. M. van Lipzig (2003), Responseof wintertime Antarctic temperatures to the Antarctic Oscillation: Results of a regional climate model, in Antarctic Peninsula Climate Variability: Historical and Paleoenvironmental Perspectives, Antarct. Res. Ser., 79, edited by E. Domack et al., pp. 43–58, AGU, Washington, D. C.

Wen, J., Y. Wang, W. Wang, K. C. Jezek, H. Liu, and I. Allison (2010), Basal melting and freezing under the Amery Ice Shelf, East Antarctica, *J. Glaciol.*, *56*(195), 81–90.

Williams, G. D., N. L. Bindoff, S. J. Marsland, and S. R. Rintoul (2008), Formation and export of dense shelf water from the Adélie Depression, East Antarctica, *J. Geophys. Res.*, *113*, C04039, doi:10.1029/2007JC004346.

Williams, M. J., K. Grosfeld, R. C. Warner, R. Gerdes, and J. Determann (2001), Ocean circulation and ice–ocean interaction beneath the Amery Ice Shelf, Antarctica, *J. Geophys. Res.*, *106*(C10), 22,383–22,399.

Wong, A. P. S, N. L. Bindoff, A. Forbes (1998), Ocean iceshelf interaction and possible bottom water formation in Prydz Bay, in Ocean, Ice, and Atmosphere Interactions at the Antarctic Continental Margin, Antarct. Res. Ser., vol. 75, edited by S. S. Jacobs and R. F. Weiss, pp. 173–187, AGU, Washington, D. C.

Yu, J., H. Liu, K. C. Jezek, R. C. Warner, and J. Wen (2010), Analysis of velocity field, mass balance, and basal melt of the Lambert Glacier–Amery Ice Shelf system by incorporating Radarsat SAR interferometry and ICESat laser altimetry measurements, *J. Geophys. Res.*, *115*, B11102, doi:10.1029/2010JB007456.

Erratum

In the originally published version of this article, the affiliations for L. Herraiz-Borreguero were incorrectly ordered. The affiliations have since been corrected, and this version may be considered the authoritative version of record.